REPORT DOCUMENTATION PAGE	*Form Approved OMB No. 0704-0188*

1. REPORT OATE *(DD-MM-YYYY)*	2. REPORT TYPE	3. OATES COVEREO *(From - To)*
9/30/13	Final Report	01/01/2006 - 06/29/2013

4. TITLE ANO SUBTITLE
CMAS DEGRADATION OF ENVIRONMENTAL BARRIER COATINGS: MECHANISMS AND MITIGATION

5a. CONTRACT NUMBER

5b. GRANT NUMBER
N00014-06-1-0322

5c. PROGRAM ELEMENT NUMBER

6. AUTHOR(S)
Carlos G. Levi
Materials Department
University of California

5d. PROJECT NUMBER
12PR03276-03

5e. TASK NUMBER

5f. WORK UNIT NUMBER

7. PERFORMING ORGANIZATION NAME(S) AND AODRESS(ES)
University of California, Santa Barbara
Materials Department, Building 503, Room 1355
Santa Barbara CA 93106

8. PERFORMING ORGANIZATION REPORT NUMBER

9. SPONSORING/MONITORING AGENCY NAME(S) ANO ADDRESS(ES)
Office of Naval Research
140 Sylvester Road

10. SPONSOR/MONITOR'S ACRONYM(S)
ONR

11. SPONSOR/MONITOR'S REPORT NUMBER(S)

12. OISTRIBUTION/AVAILABILITY STATEMENT
Distributable without limitation.

13. SUPPLEMENTARY NOTES

14. ABSTRACT

The overarching objective of this program was to develop fundamental insight into the degradation mechanisms that may limit the durability of environmental barrier coatings (EBCs) when exposed to calcium-magnesium alumino-silicate (CMAS) melts. A corollary objective was to identify strategies to enhance the environmental robustness of the underlying CMC matrix in the event of spallation or cracking of the EBC. In addition to generating fundamental understanding, the program sought to identify science-based solutions to these problems, explore their implementation and evaluate their performance in a laboratory setting.

The EBC materials of primary interest were the rare earth silicates, exemplified by Y2SiO5 (YMS) and Y2Si2O7 (YDS). A model CMAS with composition Ca33Mg9Al13Si45, used in previous ONR work, was selected for the majority of the studies. Because YMS was found to be only moderately resistant to CMAS and YDS arguably less, the overall system design may require three environmental barriers, one for oxidation (SiO2-TGO), one for volatilization (YDS/YMS) and one for CMAS (RE-zirconate or

15. SUBJECT TERMS

16. SECURITY CLASSIFICATION OF:			17. LIMITATION OF ABSTRACT	1B. NUMBER OF PAGES	19a. NAME OF RESPONSIBLE PERSON
a. REPORT	b. ABSTRACT	c. THIS PAGE			Carlos Levi
					19b. TELEPHONE NUMBER *(Include area code)* 805-893-2381

Final Report on

ONR Grant No. N00014-06-1-0322

CMAS Degradation of Environmental Barrier Coatings: Mechanisms and Mitigation

Principal Investigator:

Carlos G. Levi

Materials Department, University of California
Santa Barbara, CA 93106-5050
levic@engineering.ucsb.edu

Submitted to:

Office of Naval Research

Attention: Dr. David A. Shifler
875 N. Randolph Street, Suite 1425
ONR 332, Room 631
Arlington, VA 22203-1995

September 30, 2013

Abstract

The overarching objective of this program was to develop fundamental insight into the degradation mechanisms that may limit the durability of environmental barrier coatings (EBCs) when exposed to calcium-magnesium alumino-silicate (CMAS) melts. A corollary objective was to identify strategies to enhance the environmental robustness of the underlying CMC matrix in the event of spallation or cracking of the EBC. In addition to generating fundamental understanding, the program sought to identify science-based solutions to these problems, explore their implementation and evaluate their performance in a laboratory setting.

The EBC materials of primary interest were the rare earth silicates, exemplified by Y_2SiO_5 (YMS) and $Y_2Si_2O_7$ (YDS). A model CMAS with composition $Ca_{33}Mg_9Al_{13}Si_{45}$, used in previous ONR work, was selected for the majority of the studies. Because YMS was found to be only moderately resistant to CMAS and YDS arguably less, the overall system design may require three environmental barriers, one for oxidation (SiO_2 TGO), one for volatilization (YDS/YMS) and one for CMAS (RE zirconate or hafnate). This complex multi-layer architecture creates critical issues of thermo-chemical and thermo-mechanical compatibility when selecting system materials. The enhancement of environmental robustness of the CMC was approached by modifications of the SiC matrix and outer layer of the CMC to enable it to grow an EBC-like scale, i.e. resistant to volatilization, when exposed directly to the oxidative environment at places where the original EBC has failed. The proposed matrix compositions were also selected with due consideration to the problem of oxidation embrittlement ("pesting") of SiC CMCs at intermediate temperatures. Suitable additives are Y compounds which upon concurrent oxidation with SiC may form YMS or YDS. B additions are also expected to promote a lower temperature, fluid glass formation for enhancing resistance to oxidative embrittlement. Matrix additives explored include YB_2 in combination with Y_2O_3, Y_5Si_3 and Al_2O_3.

Progress Statement

Substantial insight was gained from the studies of CMAS interactions with EBCs, which revealed that both BSAS and YMS experienced significant degradation when exposed to the model CMAS used in this study. YMS was found to perform better than BSAS in avoiding grain boundary penetration by CMAS and forming a nearly dense layer of apatite at the reaction front, but the rate of recession at 1300°C was still deemed to be inadequate for practical applications. The lessons learned in this project were subsequently used in a study of a multilayer concept based on Yb silicates and hafnates, through an AFOSR-STTR with DVTI and Rolls Royce.

The concepts for robust matrices were largely explored on monolithic compacts produced by powder + polymer impregnation and pyrolysis (PIP) or current assisted densification (CAD) methods. It was shown that formulations based on $SiC/YB_2/Y_5Si_3/Al_2O_3$ produced scales with the desirable characteristics, comprising primarily YDS with minor amounts of YMS and YAG. It was also found that residual porosity enabled some internal oxidation that led to Y migration to the oxidizing surface, which could be desirable in crack healing scenarios but led to excessive thick scales. When density was improved by CAD the Y redistribution was largely eliminated and the thickness of the scale substantially reduced without changing its protective potential. The functionality of the concept was also demonstrated by showing that the EBC layer could be generated in a damaged area on a Si-covered matrix compact. Preliminary tests in flowing water vapor revealed enhanced thickening of the scale that suggest further refinement of the matrix chemical composition is needed. Thermodynamic measurements on the Y-B system were initiated, with the future goal of developing a thermodynamic database to guide the design of future SiC matrices with robust environmental stability. These efforts involved collaborations with Karlsruhe Institute of Technology in Germany.

Design of Multilayer Thermal/Environmental Barrier Coatings

The concept of a multilayered coating system for CMC's is motivated by the lack of a suitable material to simultaneously protect the SiO_2 thermally grown oxide (TGO) from volatilization and resist CMAS attack. The silicates of interest for EBCs have marginal to poor CMAS resistance while the rare earth zirconates (REZO[a]) that show promise for CMAS resistance must be applied with a segmented or porous structure to minimize the thermal stresses and therefore are a poor water vapor and oxidation barrier. The envisioned coating system, shown schematically in Figure 1 includes a layer of a CMAS-resistant RE zirconate/hafnate applied to a dense silicate EBC [1,2]; this coating system has been termed a T/EBC[b] due the similarity of the topcoat to conventional TBCs and the opportunity to provide thermal protection in internally cooled components.

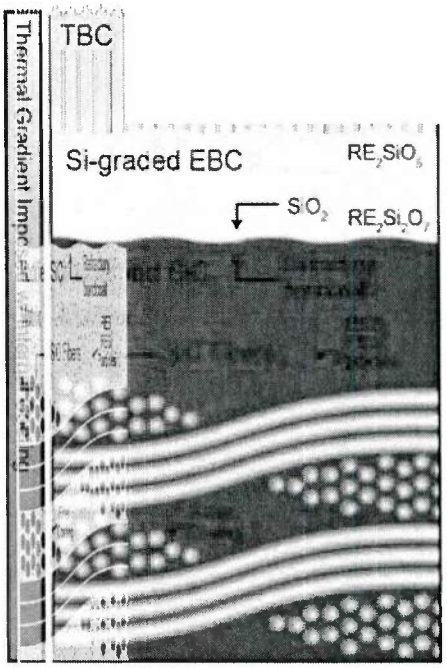

Figure 1: Envisioned robust environmental protection system for SiC based CMC including modified matrix and multilayered, multifunctional coating system.

Efforts supported by this program focused on improving the science base for designing multilayer architectures via phase equilibrium and thermo-physical property determination, thermo-mechanical modeling, and comparison of the thermal-cyclic durability and CMAS infiltration resistance of coatings produced using electron beam physical vapor deposition (EB-PVD) and current assisted densification (CAD) facilities at UCSB. The research also involved the systematic evaluation of the interaction between sintered pellets of candidate coating compositions and CMAS melts to determine the importance of factors including cation substitution and temperature on the expected performance of in-service coatings. Knowledge emerging from these activities was integrated into related efforts on TBCs under grant N00014-08-1-0522 and an AFOSR-STTR Phase II focusing on multilayer EBC systems.

Layer Architectures and Compatibility

The materials and architecture selected for the T/EBC multilayer system must satisfy multiple design criteria. Specifically, the EBC should exhibit low SiO_2 activity, be phase stable over the operating temperature range, thermodynamically compatible with the TGO and TBC, and minimize the CTE mismatch with SiC to facilitate the application of a dense coating. The outer TBC layer must also be volatilization resistant, phase stable and compatible with the EBC but the option for application of a segmented microstructure with low in-plane modulus relaxes the requirement for CTE matching. Thermochemical compatibility between the TGO and EBC is

---

[a] Oxides are abbreviated using the first letter of the cation except for Yb, The ordered pyrochlore ($RE_2M_2O_7$, RE = Gd, Nd, Sm, La) and δ ($RE_4M_3O_{12}$, RE = Yb, Y) phases with M = Zr or Hf are abbreviated REMO. Non stoicheometric compositions are reported in mole percent of oxide based on single cation formulae; for example, 20Gd-80Zr is equivalent to $20\%GdO_{1.5}+80\%ZrO_2$. The abbreviations REDS and REMS are used for $RE_2Si_2O_7$ and RE_2SiO_5, respectively.

[b] In this report the dense layer of silicate(s) serving as a water vapor barrier is referred to as the 'EBC' while 'TBC' is used to describe the segmented zirconate/hafnate layer intended to mitigate CMAS attack and provide thermal protection. These labels are based on the historic development of the separate coating concepts; functional overlap between the layers exists in the present application.

Table 1: Layer properties used in thermomechanical calculations; E and α measured in this study.

Material	Thickness (μm)	E (GPa)	□	α (ppm/K)
SiC	3000	400	0.2	5.0
SiO_2	3	67	0.2	2.0
YbDS (C2/m)	75	147	0.2	4.9
YDS ($P2_1/a$)	75	153	0.2	4.2
GdDS ($Pna2_1$)	75	172	0.2	5.4
YbMS (I2/a)	75	104	0.2	6.2
YMS (I2/a)	75	122	0.2	6.8
GdMS ($P2_1/c$)	75	148	0.2	9.3

achieved with a layer of disilicate at this interface. Preliminary evidence, however, suggests that the application of a RE monosilicate directly to the SiO_2 leads to formation of the necessary disilicate layer at the interface without compromising coating adherence. The phase equilibria between TBC and EBC materials were not studied directly under this program but based on phase equilibria in the SiO_2-$YbO_{1.5}$-HfO_2 system[2] it is assumed that monosilicates are preferred in contact with the REZO/REHO of interest to prevent detrimental interactions .

Development of RE silicate EBCs has generally focused on the smaller Lu, Yb, and Y cations to take advantage of the favorable bulk CTE of the □/5 (c2/m, $P2_1/a$) disilicate polymorphs.[3] The Lu- and Yb-systems are preferred because there are no phase transformations in the disilicates while the lower cost of YDS is desired assuming the processing route avoids the potential for phase transformation.[4] EBCs based on GdDS/GdMS have received less attention due to issues with phase transformation and CTE mismatch but were considered in the present study due to interest in Gd-based topcoat compositions.

The implications of the thermomechanical properties of proposed coating materials are often discussed in general terms but efforts to use modeling to guide the optimization of the coating architecture focused on earlier BSAS/mullite-based systems.[5] The need for improved materials property data for RE silicates and a framework for modeling multilayer EBCs were addressed under this program. The average bulk CTE and modulus (E) for Yb, Y, and Gd mono- and di-silicates were measured using dilatometry and nancindentation, respectively. The results of these measurements are reported in Table 1; these values are generally in agreement with properties previously reported in the literature. The CTEs for the disilicates are closely matched to SiC with YDS slightly lower and GdDS slightly higher than SiC. The CTEs for the monosilicates are significantly higher than SiC and increase with RE cation radius. The modulus for both families of silicates increases with the RE cation size. These material properties and the coating parameters listed in Table 1 were used for the thermomechanical modeling.

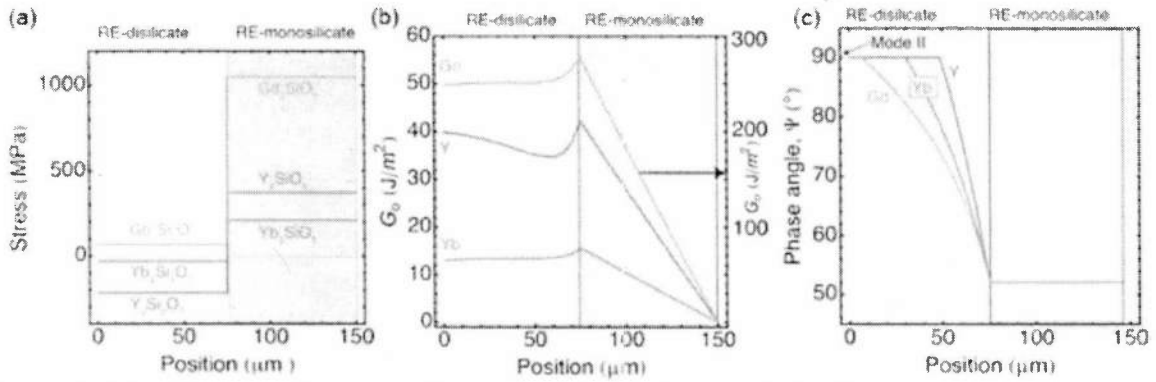

Figure 2: The (a) stress, (b) energy release rate, (c) and phase angle for bilayer Y,Yb, and Gd-DS/MS coatings on SiC cooled from 1400°C. (NB, in (b) G_o for the Gd silicate system, labeled on the left ordinate axis are a factor of five greater than for Y- and Yb-silicates, labeled on the left ordinate)

The T/EBC layers are inherently prone to degradation by cracking during thermal cycling due to the CTE mismatch between coating and substrate. The variation in properties between coating layers has a strong influence on the expected crack pattern. Considering first the simplest case of monolayer coatings cooled from a relaxed stress state at the deposition or operation temperature, YbDS and YDS coatings will be under compression that could lead to edge delamination or buckling dependent on the size of interface flaws, the interface toughness, and the coating thickness. Monolayer coatings of GdDS and all monosilicates are expected to be in tension during cooling leading to Mode I channel cracks that could, based on mode mixity for a specific case, deflect along the interface leading to coating delamination.

The more relevant case for the development of T/EBC architectures is the stress state a bilayer DS||MS EBC. The mechanics of thermally cycling this architecture were analyzed based on the work of Evans, Suo, He, and Hutchinson.[6-9] The stress within the individual layers, shown in Figure 2(a), is equivalent to the case of monolayers of the respective materials. For the Yb and Y coatings, the stress shifts from compression to tension at the DS||MS interface. The maximum energy release rate (ERR), Figure 2(b), is located at the MS/DS interface. For the Gd coatings, both the DS and MS layers are in tension, however, the maximum ERR remains at the DS/MS interface. For delamination in the MS layer, the fracture is mixed mode but the phase angle remains constant. Within the DS layer the phase angle is depth dependent, and as shown Figure 2(c), increases through the layer thickness and is entirely Mode II by the TGO||DS interface.

A free edge must be present for delamination cracks to propagate in the bilayer coating. The most probable source of a free edge is a channel crack. Channel cracks initiated at the coating surface will propagate unstably into the coating if the coating is in a state of residual tension. Thus, cracks are expected to propagate through Gd-silicate bilayer to the SiC substrate and from the outer MS surface to the MS||DS interface in the Yb/Y systems. At the interface, the crack can arrest, penetrate into the layer below, or deflect along the interface. It is therefore most likely for delaminations to form at any location in the Gd-silicate coating. In Y/Yb-based coatings, edge delamination is most likely to initiate in the MS layer, near the MS||DS interface. In this scenario, the crack will grow stably into the compressive film and the penetration depth will be determined by stored energy in the coating.

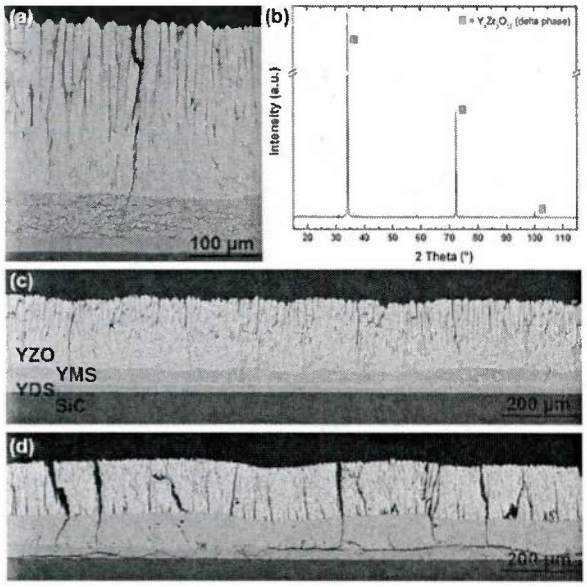

Figure 3: Multilayer YDS||YMS||YZO T/EBC applied to monolithic SiC. (a-c) show microstructures and XRD in as-deposited condition. The microstructure after 200 1h cycles to 1400°C is shown in (d).

This analysis suggests that the combination of well-matched CTE and comparatively low moduli make Yb-based EBCs most resistant to thermomechanical damage in the configuration considered, and that the stress/ERR for the Gd-based system is unacceptably high. Channel cracks are most likely to form in the outer MS layer and these cracks could either extend into the DS layer or deflect along the DS||MS interface. Although this modeling considered a single coating geometry with different material properties, the methods developed can be used in future studies to optimize the architectures to minimize the peak ERR to improve coating durability.

To validate the conclusions of the modeling activities, bilayer EBCs and trilayer T/EBCs based on the Yb, Y, and Gd systems were produced. Isothermal and cyclic heat treatments were used to assess the relative durability of the architectures. SiC disks containing 5wt% $YO_{1.5}$ sintering aid were produced by CAD for use as substrates for coating deposition. The EBC layers were applied by spreading slurries of the respective silicates onto the substrate. Following binder burnout the layers were co-sintered and bonded to the substrate by CAD. There was generally limited evidence of cracking following EBC sintering for the Yb-based system and moderate channel cracking in the Y-based system. It was not possible to produce a dense GdDS||GdMS bilayer without delamination and spallation of the coating consistent with the higher calculated ERR; as a result it was impractical to produce trilayer Gd-based architectures.

The outer zirconate layers were deposited by EB-PVD using ingots with the nominal composition $RE_4Zr_3O_{12}$. Figure 3 (a,c) shows the typical as-deposited structure for the YDS||YMS||YZO coating system. Channel cracks, formed when the specimen was cooled from the deposition temperature, penetrate through the YZO and YMS layers and appear to arrest at the YDS||YMS interface consistent with tension in these layers upon cooling. The architectures appear to be relatively stable during isothermal heat treatment. During thermal cycling, however, the deflection of the channel cracks, visible in Figure 3 (d), along the interfaces or through the YDS layer ultimately compromises the integrity of the coatings. The equivalent Yb-based coating, not shown, suffered from enhanced sintering in the YbZO leading to additional channel cracking in this layer. These sintering-induced cracks deflect along the YbMS||YbZO interface and eventually link causing local delamination of the outer layer. It is currently not clear whether the difference in sintering behavior is inherent to the coating composition or instead related to differences in the as deposited coating microstructure (e.g. column spacing, size). While the program did not permit the refinement of the processing methods or optimization of the layer architecture for extended performance, the initial results are an important proof the T/EBC concept.

Factors Influencing the CMAS-resistance of RE Zirconates and Hafnates

The interaction between a CMAS deposit and T/EBC system would ideally be confined to the outer layer without degrading the performance of the EBC or CMC. Suitable materials for the TBC layer must be able to arrest the silicate melt penetration into open features in the coating. Conventional TBC compositions such as 8YSZ are not suitable for the T/EBC application.[10] Previous ONR efforts, however, revealed that at 1300°C zirconates with a higher rare earth cation fraction limit infiltration by crystallizing the melt through a sequence of rapid dissolution/precipitation reactions. This process is exemplified by $Gd_2Zr_2O_7$ (GZO) coatings that form a Ca:RE apatite silicate, nominally $Ca_2Gd_8(SiO_4)_6O_2$, that blocks open passages in the microstructure.[11] The dissolved ZrO_2 re-precipitates as a Gd-lean cubic fluorite phase and the Si- and Ca-depleted melt converts to crystalline silicates with little or no Gd. Studies involving EB-PVD and APS coatings and sintered pellets of TBC compositions provide evidence that this reactive crystallization process is active in other rare earth zirconates.[11-13] The current program further developed the fundamental understanding of reactive crystallization in two key areas related to the design of T/EBCs. First, the effect of changing the reactive cations on the interaction with CMAS melts was studied. Second, the potential for utilizing reactive crystallization to mitigate CMAS attack at 1500°C, the surface temperatures envisioned for coated CMCs, was investigated.

Because phase stability and thermomechanical considerations preclude the use of Gd-silicate EBCs, T/EBCs with the architecture YbDS||YbMS||YbHO have been considered to avoid potential compatibility issues with a GZO TBC applied directly to a Yb-silicate EBC.[2] Experiments on coatings in this system, however, revealed that the CMAS/YbHO interaction at 1300°C did not prevent penetration of the silicate melt into the intercolumnar gaps.[14] The inferior behavior of the Yb-based TBC relative to GZO is apparently associated with diminished formation of the desira-

ble apatite phase. Further analysis of the YbHO system, supported by this program, revealed that a portion of the $YbO_{1.5}$ dissolved into the melt promotes the crystallization of a garnet silicate that grows too slowly to arrest CMAS infiltration. Additionally, the $YbO_{1.5}$ concentration in the reprecipitated fluorite is higher than the comparable phase in the GZO system. As a result, additional coating dissolution and/or a higher $YbO_{1.5}$ composition in the original coating is required to form an equivalent volume of apatite.[14]

If it is assumed that the coating behavior is dictated by the RE cation, the results for the YbHO system contradict work suggesting that YbZO resists infiltration better than GZO by generating more apatite per mole of dissolved coating.[12] The earlier finding was rationalized by considering the crystal chemistry of the apatite phase, represented by the formula $M^{I}_4M^{II}_6(SiO_4)_6O_x$ where the 9-fold coordinate M^{I} sites may accommodate larger cations than the 7-fold coordinate M^{II} sites. In the case of the apatite formed during CMAS/GZO reactions, the Gd cation is sufficiently large to occupy a fraction of the M^{I} sites. Drexler et al. hypothesized that the smaller Yb cations should be less likely to occupy the M^{I} site, increasing the Ca consumed from the melt, $Ca_4Yb_6(SiO_4)_6O$ vs. $(Ca_2Gd_2)Gd_6(SiO_4)_6O_2$, but the actual composition of the apatite formed during the CMAS/YbZO interaction was not reported.[12]

A systematic comparison was made between Yb, Gd, and La zirconate and hafnate phases to clarify the role of the RE cation radius on the apatite chemistry and assess whether subtleties in the reactions with ZrO_2 vs. HfO_2 systems influence the composition of the reaction products. Experiments were performed on sintered pellets of the respective compositions using powders synthesized by reverse co-precipitation.[2] Crystalline CMAS with the nominal composition 33Ca–9Mg–13Al–45Si and a melting temperature of ~1235°C was used for consistency with related studies.[10,11] Thin CMAS disks were prepared as described by Grant et al.[15] to achieve an areal loading of 15±2 mg/cm^2. The CMAS wafers were placed in the center of the specimen and the assemblies were annealed for 4h at 1300°C, enabling comparison with the TBC literature, or 1500°C, which is more relevant for the T/EBC application.

The characterization of the mechanism(s) of attack and identification of reaction products involved a combination of microstructure, crystallographic and composition data to develop a clear understanding of the phenomena relevant to the design of engineered coatings. The specimens were first analyzed via XRD and SEM. TEM lamellae were extracted from representative regions using focused ion beam (FIB). Selected area electron diffraction (SAED) was employed to confirm the crystal structure of select reaction products. Due to small grain size, the compositions of the apatite and fluorite reaction products were determined primarily using energy dispersive spectroscopy in the TEM (TEM-EDS). The RE, Zr, Hf, and Ca concentrations were calibrated with REZO/REHO and amorphous CMAS standards verified by inductively coupled plasma mass spectrometry (ICP-MS). Because of overlap between the Mg-, Al-, and Si-K energies and the Yb- and Hf-M energies in EDS, selected larger grains were analyzed using EPMA. The TEM-EDS peak areas for the phases analyzed by EPMA were matched with the spectra from other locations/specimens to aid the identification of equivalent phases with grains too small to analyze by EPMA.

Figure 4 and Figure 5 show the microstructures of the interaction zones under the CMAS deposit for each composition tested at 1300°C and 1500°C, respectively. The identity and measured compositions of the primary reaction products are reported in Table 2 and Table 3. At 1300°C residual glass is evident on the surface of each pellet and the infiltration into the open porosity extends no more than few tens of microns below the original pellet surface. The reaction products formed for the Yb-based compositions include apatite, fluorite and garnet. Near the advancing dissolution/reprecipitation front the faceted apatite and globular fluorite grains, all of order 1μm, are suspended in much larger garnet grains suggesting that the latter form more

slowly, engulfing the finer grains as it grows outward. The reaction products for both Gd-based compositions include apatite and fluorite. Interaction with the GHO produces the lowest volume fraction of crystalline reaction products although the increased interaction with the GZO may be due in part to increased porosity, and therefore open surface area, in the original pellet. The volume of residual glass is lowest for the La-based materials suggesting that these compositions may be most effective in crystallizing the melt. For LZO the primary reaction products are again apatite and fluorite, but unlike the Yb- and Gd-based systems the fluorite is stabilized primarily by Ca rather than La. The CMAS/LHO reaction produces apatite and monoclinic HfO_2 with negligible Ca or La solubility.

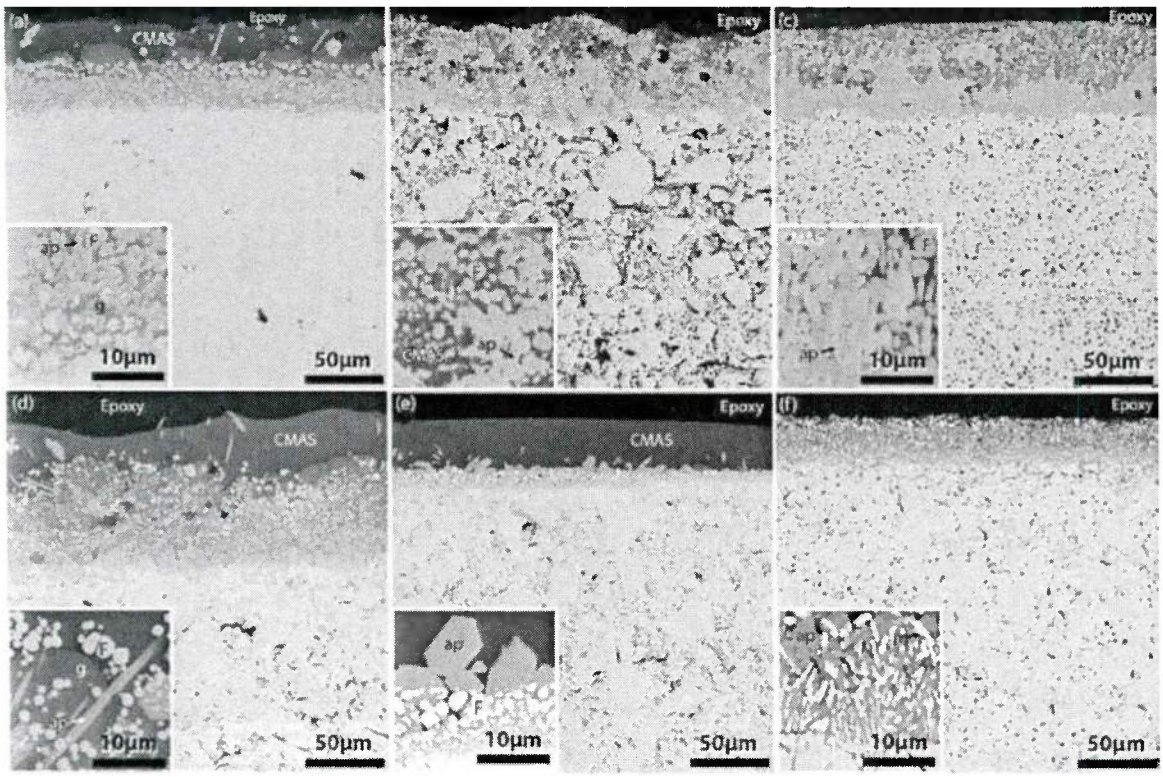

Figure 4: Microstructure of the region of interaction between molten CMAS and sintered pellets of (a) YbZO, (b) GZO, (c) LZO, (d) YbHO, (e) GHO, and (f) LHO after 4h at 1300°C. The insets show the representative microstructure near the advancing reaction front. Phases are labeled according to Table 2; additional discussion and comparison of the microstructure features is included in the text.

Following 4h at 1500°C, Figure 5, there is no residual CMAS glass. Silicate grains are observed further below the pellet surface than at 1300°C. In addition to apatite, present in all specimens, a second $YbO_{1.5}$-rich silicate was observed. This phase is identified as a sorosilicate in the cuspidine family, nominally $A_4(T_2O_7\square)X_2$.[16] The A cations, typically Ca or RE, occupy a nominally octahedral site, the tetrahedral T site incorporates Si and/or Al, and X can include F, OH, N, and/or O. Compositional flexibility is enabled by the accommodation of oxygen anions between the T_2O_7 groups in the site denoted '$\square$'. Based on the crystal chemistry and EPMA measurements (Table 3), the tentative composition is $(Yb_{0.63}Ca_{0.26}Mg_{0.07}Hf_{0.04})_4((Si_{0.77}Al_{0.23})_2O_7O_{0.18})O_2$. Excluding the minor HfO_2 and MgO content, this phase is effectively a quaternary solid solution between a calcium silicate[17], $Ca_4(Si_2O_7)(OH)_2$, and ytterbium aluminate, $Yb_4(Al_2O_7)O_2$

(YbAM)[18,19]. The latter is structurally equivalent to the more familiar $Y_4Al_2O_9$ (YAM) phase, which has been reported to have ~18mol% SiO_2 solubility[20].

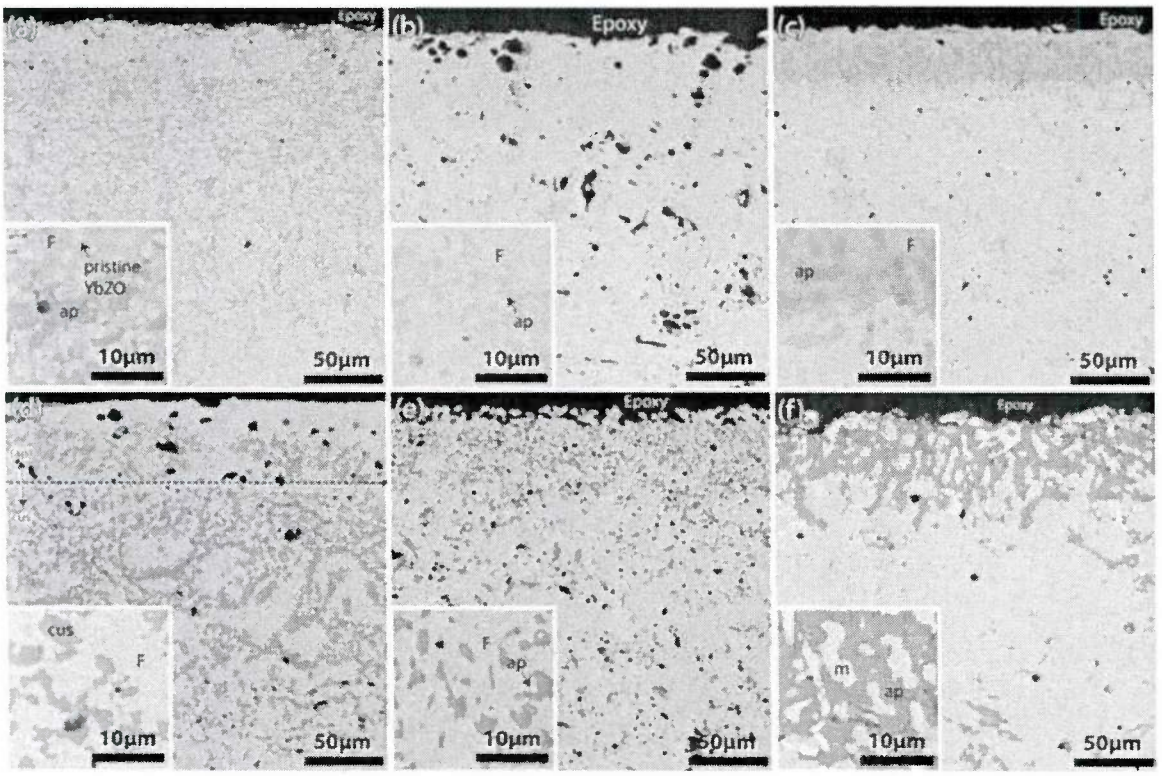

Figure 5: Microstructure of the region of interaction between molten CMAS and sintered pellets of (a) YbZO, (b) GZO, (c) LZO, (d) YbHO, (e) GHO, and (f) LHO after 4h at 1500°C. The insets show the representative microstructure features approximately 50μm below the surface. Phases labeled according to Table 2. The dashed line in (d) indicates the apparent transition from apatite to U2 as the primary silicate reaction product, determined by EPMA.

The more severe interaction at 1500°C is consistent with increased reaction and penetration rates and an evolution in the equilibrium phases as the temperature is increased. The interaction is generally divided into two zones. Near the surface a layer 25μm-50μm thick is characterized by dissolution of the pellet material and precipitation of a significant volume fraction of silicate reaction products. This layer is most evident for the La-based composition due to favorable contrast between the phases but EPMA measurements and TEM analysis suggest that similar layers exist in the other specimens. Increasingly sporadic silicate grains surrounded by zirconate/hafnate material partially depleted in RE relative the reprecipitated grains near the surface extend several hundred microns below this layer. In the envisaged reaction sequence, the CMAS begins to infiltrate into open porosity in the pellets when the melt forms. The penetrating melt becomes increasingly enriched in RE until it is sufficiently saturated to precipitate a crystalline silicate, slowing the infiltration and leaving a thin layer of CMAS on the surface. This residual melt is consumed through dissolution/reprecipitation reactions due to the accelerated reac-

Table 2: CMAS reaction product abbreviations

Phase	Description
F	Ca and RE stabilized cubic ZrO_2/HfO_2
m	Monoclinic HfO_2
ap	RE/C-silicate apatite
g	RE/CMA-silicate garnet
cus	RE/CA-silicate cuspidine

Table 3: Measured reaction product compositions in pellet-based CMAS/TBC experiments.

Pellet Composition	Temp. (4h)	Reaction Products	MO_2-Based (cat%)			Apatite (cat%)			
			Hf/Zr	RE	Ca	Si	Hf/Zr	RE	Ca
YbHO	1300°C	F+ap+g	62	37	1	37.5[c]	2	47	14
YbZO	1300°C	F+ap+g	67	32	1	37.5[c]	2	46	15
GdHO	1300°C	F+ap	73	21	7	36	2	48	14
GdZO	1300°C	F+ap	78	17	5	36	3	45	16
LaHO	1300°C	m+ap	99	1	0	36	1	49	14
LaZO	1300°C	F+ap	83	3	14	36	1	50	13
YbHO[a]	1500°C	F+ap+cus	53	46	1	36	3	48	13
YbZO	1500°C	F+ap+cus	56	43	1	37.5[c]	2	47	14
GdHO	1500°C	F+ap	55	42	3	37	1	48	14
GdZO	1500°C	F+ap	59	37	4	36	1	51	12
LaHO	1500°C	m+ap	100	0	0	38	1	50	12
LaZO	1500°C	F+ap	81	8	11	38	1	48	13
			Ca	Mg	Al	Si	Yb	Hf	
46Hf-54Yb[c]	1300°C	garnet	25	14	13	35	11	3	
46Hf-54Yb[c]	1500°C	cuspidine	18	4	8	26	42	3	

[a] Compositions determined by EPMA; limited overlap with adjacent grains possible.
[b] Due to overlap between Yb-M and Si-K energies composition computed assuming 6 Si cations per formula unit.
[c] EPMA measurements; compositions of respective phases assumed to be similar in other instance (i.e. g in YbZO)

tion rate at the higher temperature. In this sequence, the phases present closest to the surface presumably better represent the pseudo-equilibrium between the melt and crystalline reaction products while the partially depleted zirconate/hafnate phases present further below the surface arise from transient interaction with the penetrating melt.

The salient findings of the pellet-based experiments are derived from the relative distribution of the constituents of the zirconate/hafnate and CMAS melt between the reaction products. In the ideal scenario, a low ratio of RE to Zr/Hf in the reprecipitated fluorite maximizes the RE available to crystallize the melt while a high fraction of Ca in the apatite increases the volume of the apatite formed. The solubility of Ca in fluorite and Zr/Hf in apatite, while limited, further promote crystallization. The measured compositions of the respective phases are plotted in based on these relationships in Figure 6. Several trends are evident for the reprecipitated ZrO_2/HfO_2, Figure 6(a). First, the concentration of RE decreases with increasing RE cation radius such that at 1300°C almost half of the Yb is retained in the reprecipitated phase while for the La-based systems there is essentially no La in the reprecipitated fluorite; this trend is magnified at 1500°C. The RE concentration is generally slightly lower for the zirconates than the hafnates under equivalent conditions but this effect is less pronounced than that of either temperature or RE cation radius. Conversely, there is no apparent trend in the apatite composition as a function of either temperature or pellet composition. Instead, all measured apatite compositions fall near the ratio Ca:RE~4, Figure 6(b). The reported reaction product compositions for experiments on coatings based on various RE cations, also plotted in Figure 6, support the trends in the pellet-based experiments. It is not immediately evident whether these results are explicitly tied to the equilibrium between the respective apatite and fluorite phases, and therefore independent of the CMAS composition, or instead related to the kinetics of the growth for each phase, making them dependent on the melt chemistry. These questions deserve attention in future studies.

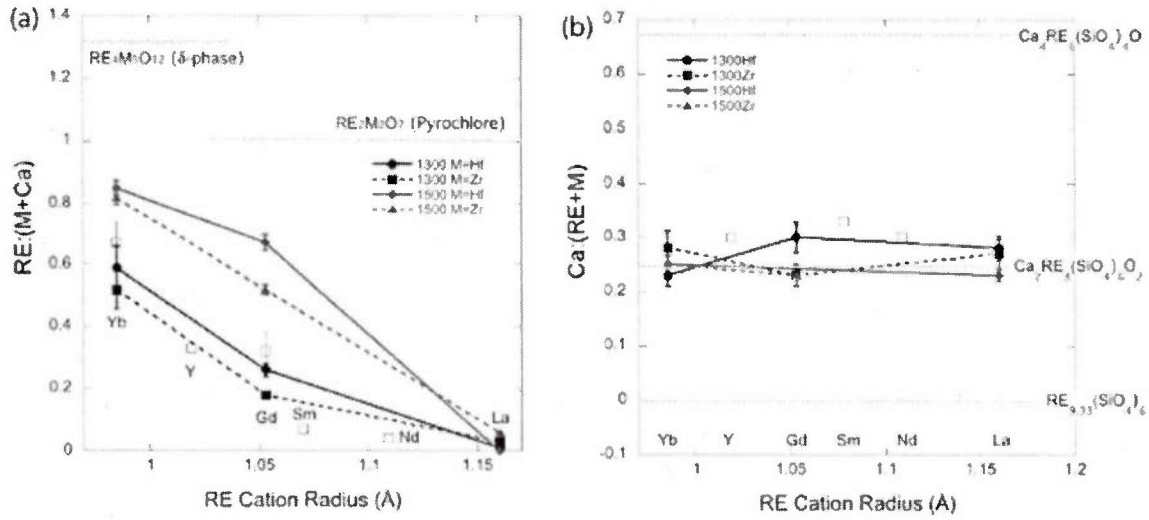

Figure 6: Composition of the (a) reprecipitated MO_2 and (b) precipitated apatite phases formed during the interaction of CMAS with sintered pellets of REMO at 1300°C and 1500°C. Open symbols represent comparable experiments performed on EB-PVD coatings including YbHO at 1300°C[14], YZO at 1300°C [21], GZO at 1300°C [11], SZO at 1250°C [22], and NZO+CAS at 1200°C [23]. Dotted lines in (a) represent the ratio for the respective starting compositions while those in (b) represent the limits of Ca solubility in apatite based on crystal chemistry and the nominal $Ca_2Re_2(SiO_4)_6O_2$ composition expected to form when CMAS-type melts interact with TBC and EBC materials.

The results carry important implications for the design of CMAS-resistant coatings. The conventional wisdom in the literature describing RE zirconate/CMAS interaction is that there is limited competition for the RE cation between the precipitating fluorite, apatite, and other reaction products. It has been proposed that apatite grows in local equilibrium with the RE-enriched melt and that the RE content in the fluorite is a reflection of the excess dissolved RE not consumed through apatite precipitation. This understanding is based on the range of theoretical RE solubility in ZrO_2-fluorite and the variation in the reprecipitated fluorite composition as a function of the measurement location relative to the initial coating structure [11]. This study, however, reveals that absent the effects of a coating microstructure there is competition for the RE between the precipitating silicate and ZrO_2/HfO_2 grains. In combination with the apparent temperature and composition insensitivity of the apatite chemistry, the results suggest that coatings based on the larger RE cations should offer benefits at higher temperatures and in coatings with lower bulk RE concentration.

The pellet-based experiments suggest that as the temperature is increased the RE is less potent in crystallization reactions, manifested as higher RE concentrations

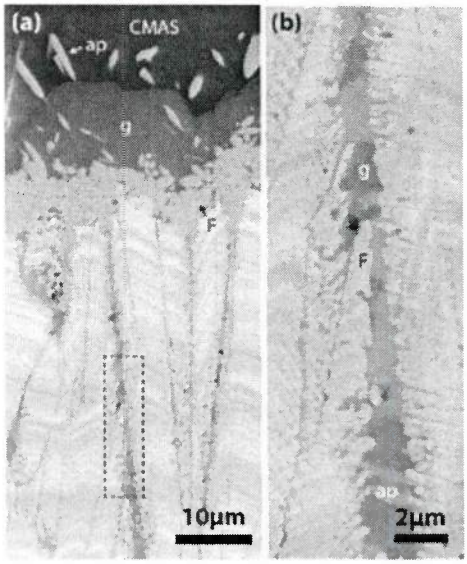

Figure 7: CMAS infiltration into intercolumnar gaps in the EB-PVD YbZO coating. The large garnet grains at coating surface in (a) are similar to those observed in the pellet-based tests. The limited volume of apatite formed in the gaps (b) does not efficiently block penetration.

in the reaction products. These experiments do not, however, adequately capture the role of increased dissolution rate on the ability of the interaction to block infiltration channels. Specifically, faster dissolution of the coating could partially counteract the lower viscosity and the requirement for additional RE by liberating more RE early in the reaction sequence. To evaluate the effectiveness of pellet-based screening tests in predicting the performance of a coating system and validate this CMAS mitigation concept, the CMAS resistance of T/EBCs with columnar YbZO, YZO, and GZO outer layers was studied. These coating architectures were produced using the methods described earlier and consisted of Yb- and Y-silicate bilayer EBCs on monolithic SiC with either a single layer of the corresponding zirconate or a bilayer YbZO||GZO or YZO||GZO TBC.

Coatings with YbZO or YZO topcoats were only moderately effective in mitigating the infiltration of the CMAS melt. At 1300°C the melt penetration extended several tens of microns down the intercolumnar gaps in the YbZO coatings, shown in Figure 7, with slightly less penetration in the equivalent YZO coatings. As predicted by the pellet-based tests, apatite and fluorite formation on the YbZO system appear to be secondary to the growth of large garnet grains that fill the gaps and extend into the residual melt at the surface of the coating. At 1500°C the silicate melt penetrated deeper into the zirconate layer and reaches the EBC layer in multiple locations across the analyzed cross sections. In an attempt to improve the resistance of the TBC layer against CMAS infiltration while maintaining the desired Yb- or Y- based EBC architecture, an outer layer of GZO was applied to the YbZO/YZO coatings. This configuration is preferred over applying GZO directly to the Yb/Y silicate because the exchange of RE cations within the TBC layer is arguably less detrimental than across the TBC||EBC interface. As shown in Figure 8 for the YZO-based system, this architecture resists CMAS infiltration at 1300°C. Following the 4h/1500°C exposure, the entire GZO layer has reacted with the CMAS melt; this dense layer is likely prone to exfoliation during thermal cycling but the retention of the columnar structure in the YZO layer is preferred to complete penetration of the TBC observed following 1500°C exposure in architectures without the GZO capping layer.

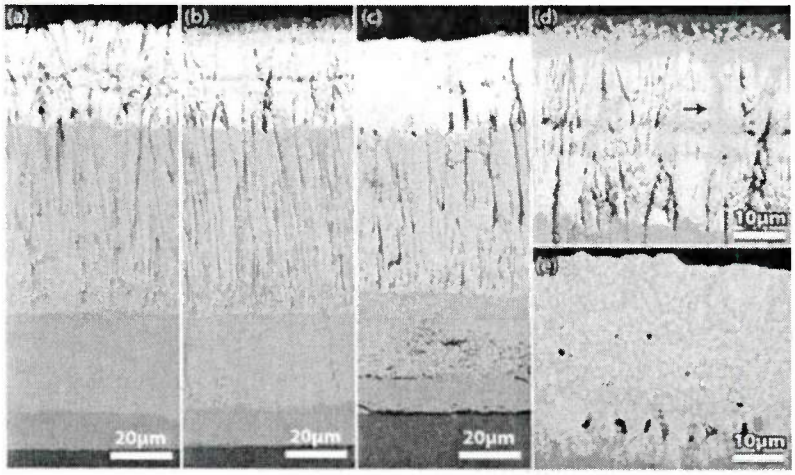

Figure 8: Multilayer T/EBC with architecture YDS||YMS||YZO||GZO on monolithic SiC in (a) as deposited condition and after CMAS exposure for 4h at (b) 1300°C and (c) 1500°C. (d) At 1300°C the silicate melt is generally confined to a layer approximately 10μm thick at the surface of the GZO although deeper penetration occurs along coating features that offer a wider channel for infiltration, indicated by the arrow. At 1500°C (c, e) there is evidence of significant dissolution such that the original columnar GZO structure is not evident. Penetration generally extends into the YZO layer but only reaches the YMS in locations where coating defects provide a wide channel for infiltration.

The GZO-capped coating structures illustrate the role of coating chemistry on the effectiveness of the reactive crystallization process, but the discontinuity in the columnar structure at the transition complicates the analysis. To further evaluate the role of temperature in the reaction process experiments were performed using bilayer EB-PVD YSZ||GZO coatings on

polycrystalline alumina substrates to build upon experience with GZO at 1300°C using heating rates of 6°C/min [11] and 10°C/min [24]. After exposure to CMAS for 4h at 1500°C using 10°C/min heating and cooling rates evidence of interaction with the melt was observed through the coating thickness for the majority of the column gaps, Figure 9(c), with more significant degradation evident in the vicinity of coating defects creating wider column gaps.

Examination of the microstructure of an infiltrated column gap and adjacent column by TEM, Figure 10, revealed that apatite is the primary reaction product. Unlike the combination of fine apatite and fluorite grains surrounded by residual CMAS glass observed at 1300°C in the inter-columnar space, however, the microstructure at 1500°C consists of larger apatite grains with limited occurrence of the globular fluorite morphology. The composition gradients across the retained column material are consistent with solid-state diffusion of Gd cations from the coating into the melt and corresponding Ca enrichment of the undissolved column. Adjacent the apatite, the zirconate is depleted in $GdO_{1.5}$ by approximately 10mole% relative to the core of the column. The regions closest the apatite filled channel contain approximately 3mol% dissolved CaO while the apparent center of the column contains <1 mol% CaO. The measured CaO concentrations are plotted in Figure 10(b) as a function of the distance from the edge of the bulk apatite. The Ca diffusion length suggested by these measurements is similar to the diffusion profile calculated for 4h/1500°C using data for Ca diffusivity in YSZ [25].

Comparison of the expected Ca composition profile across a 7.5μm diameter cylindrical column after 4h at 1300°C and 1500°C, both shown in Figure 10(b) suggests that at 1300°C Ca accumulation, and presumably Gd depletion, in the fluorite occur primarily through dissolution and reprecipitation while at 1500°C it is plausible that there is a significant contribution from solid state diffusion. In the envisioned reaction sequence, the penetrating melt initially dissolves the feathery features adjacent the gap producing apatite and a thin layer of fluorite depleted in $GdO_{1.5}$ and enriched in CaO relative to both the initial coating composition measurements after 4h/1500°C exposure. Once the CMAS is consumed, stopping the reaction, diffusion redistributes the Gd and Ca cations to reduce the composition gradient across the undissolved column. This result is supported by measurements following the 20min/1500°C exposure that reveal higher CaO and lower $GdO_{1.5}$ concentrations near the apatite after the shorter interaction time.

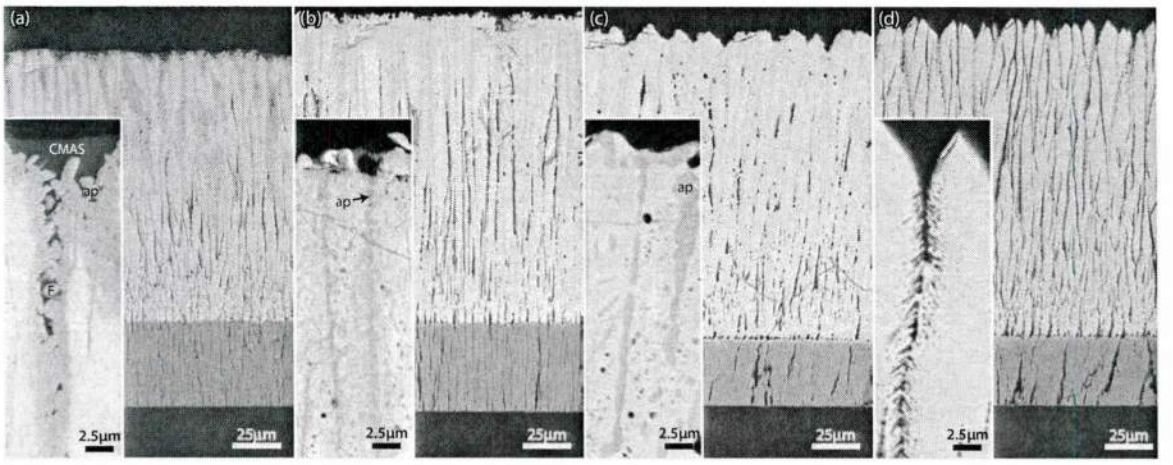

Figure 9: SEM micrographs of GZO/YSZ multilayers illustrating the effect of thermal history on the interaction with CMAS: (a) 1300°C/20min, (b) 1300°C/20min+1500°C/15min, (c) 1500°C/4h, and (d) 1500°C/4h. Heating rates and additional description provided in the text.

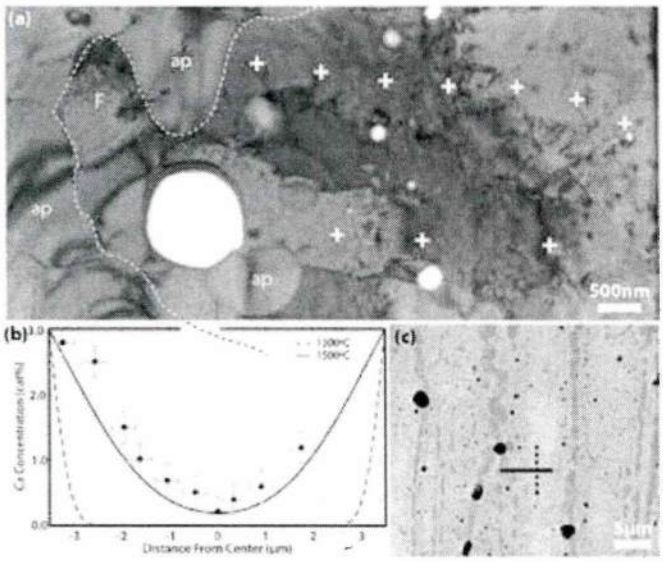

Figure 10: (a) BF TEM micrograph of GZO coating following 1500°C/4h CMAS exposure showing an apatite-filled intercolumnar gap and adjacent column. The lamella was extracted from the area marked by the solid black line in (c). TEM-EDS measurement of the Ca concentration in the locations marked by '+' are plotted in (b) as a function of the distance from the edge of the primary apatite grains, indicated by the dashed line in (a). The column center, marked by the dashed vertical line in (c), is inferred based on the minimum Ca concentration and agrees with the total column width measured in (c). The Ca composition profile across the column was calculated using Ca diffusivity data for YSZ [25].

While these results reveal that reactive crystallization is not sufficiently fast to arrest melt penetration, the presence of apatite in the intercolumnar gaps suggests that apatite is stable and can fill column gaps at 1500°C. It appears that performance is limited by the faster infiltration kinetics due to the lower CMAS viscosity at 1500°C rather than an inherent deficiency in the apatite chemistry. It is therefore plausible that a blocking layer formed at a lower temperature could be effective in preventing penetration at a higher temperature. This scenario if particularly relevant to aero turbines, which typically operate below the peak temperature for long periods; important therefore to determine whether a coating exposed to CMAS at a lower temperature, such as during cruise, can then survive short excursions to higher temperatures experienced during takeoff and climb.

To address these questions additional experiments were performed using GZO coatings. Sister specimens underwent 20min/1300°C CMAS exposures using fast (>1°C/s) heating from 1150°C to the 1300°C to minimize transient effects. The first specimen was extracted from the furnace after the 1300°C dwell and the second was heated at >1°C/s to 1500°C and held for an additional 15min. The coating tested only at 1300°C, shown in Figure 9 (a), exhibits deeper penetration of the column gaps that reported for slower heating rates [11,24] This suggests that the CMAS resistance reported at 1300°C may be due in fact to reactions between the coating and melt in the moments after the melt forms and before the specimen reaches the intended test temperature. Nonetheless, the crystallization of the melt in the channels ultimately blocks the infiltration leaving a thin layer of CMAS on the specimen surface. After the short exposure at 1500°C, Figure 9(b), the residual melt is consumed and there is evidence of further penetration into the coating but the performance with the short 1300°C pretreatment is arguably better than heating the specimen directly to 1500°C (cf. Figure 9(b,c)). The additional penetration observed after the 1300°C pretreatment may result from the dissolution of a small fraction of the reaction products into the residual melt due to higher $GdO_{1.5}$ solubility as the temperature is increased. Reaction at an intermediate temperate is therefore expected to be most effective at protecting the coating at higher temperatures if the entire melt is consumed at the lower temperature.

Broader Impacts

The work funded under this program has contributed to the understanding of the degradation mechanisms for conventional EBC materials and has identified viable solutions to mitigate these

mechanisms. Multilayer T/EBCs are proposed to address the poor resistance of silicate EBCs to attack by molten silicate (CMAS) deposits. Thermo-chemical and thermo–mechanical considerations point toward the use of systems based the smaller rare earth cations (e.g. Yb), but it was demonstrated coatings based on the larger RE cations (e.g. Gd, La) are better suited to prevent the infiltration of a CMAS melt. Specific attention was focused on improving the understanding of the CMAS penetration and reaction sequence in GZO coatings at 1500°C to complement previous work with this system at lower temperatures. The results lay the foundation to optimize these multilayer architectures in future programs.

References

1. I. Spitsberg and J. Steibel, "Thermal and Environmental Barrier Coatings for SiC/SiC CMCs in Aircraft Engine Applications," *The International Journal of Applied Ceramic Technology,* **1[4]** 291-301. (2004).
2. D.L. Poerschke, K.B. Wong, J.S. Van Sluytman, and C.G. Levi, "Thermochemical Compatibility of Ytterbia-(Hafnia/Silica) Multilayers for Environmental Barrier Coatings," *Acta Mater.,* **61[18]** 6743-6755. (2013).
3. A.J. Fernández-Carrión, M. Allix, A.I. Becerro, and M. White, "Thermal Expansion of Rare-Earth Pyrosilicates," *J. Am. Ceram. Soc.,* **96[7]** 2298-2305. (2013).
4. J. Felsche, "Polymorphism and crystal data of the rare-earth disilicates of type $RE_2Si_2O_7$," *Journal of the Less Common Metals,* **21[1]** 1-14. (1970).
5. A. Abdul-Aziz and R.T. Bhatt, "Modeling of thermal residual stress in environmental barrier coated fiber reinforced ceramic matrix composites," *J. Compos Mater.,* **46[10]** 1211-1218. (2011).
6. Z.G. Suo and J.W. Hutchinson, "Interface Crack between 2 Elastic Layers," *Int J Fracture,* **43[1]** 1-18. (1990).
7. A.G. Evans, B.J. Dalgleish, M. He, and J.W. Hutchinson, "On Crack Path Selection and the Interface Fracture Energy in Bimaterial Systems," *Acta Metallurgica,* **37[12]** 3249-3254. (1989).
8. A.G. Evans, M.Y. He, and J.W. Hutchinson, "Interface Debonding and Fiber Cracking in Brittle Matrix Composites," *J. Am. Ceram. Soc.,* **72[12]** 2300-2303. (1989).
9. J.W. Hutchinson and Z. Suo, "Mixed-Mode Cracking in Layered Materials," *Adv Appl Mech,* **29** 63-191. (1992).
10. S. Krämer, J. Yang, C.G. Levi, and C.A. Johnson, "Thermochemical Interaction of Thermal Barrier Coatings with Molten CaO–MgO–Al_2O_3–SiO_2 (CMAS) Deposits," *J. Am. Ceram. Soc.,* **89[10]** 3167-3175. (2006).
11. S. Krämer, J. Yang, and C.G. Levi, "Infiltration-Inhibiting Reaction of Gadolinium Zirconate Thermal Barrier Coatings with CMAS Melts," *J. Am. Ceram. Soc.,* **91[2]** 576-583. (2008).
12. J.M. Drexler, A.L. Ortiz, and N.P. Padture, "Composition effects of thermal barrier coating ceramics on their interaction with molten Ca-Mg-Al-silicate (CMAS) glass," *Acta Mater.,* **60[15]** 5437-5447. (2012).
13. N.K. Eils, P. Mechnich, and W. Braue, "Effect of CMAS Deposits on MOCVD Coatings in the System Y_2O_3–ZrO_2: Phase Relationships," *J. Am. Ceram. Soc.,* **96[10]** 3333-3340. (2013).
14. D.L. Poerschke, D.D. Hass, S. Eustis, G.G.E. Seward, J.S. Van Sluytman, and C.G. Levi, "Stability and CMAS Resistance of Ytterbium-Silicate/Hafnate EBCs/TBC for SiC Composites," *J. Am. Ceram. Soc.,* **98[1]** 278-286. (2015).
15. K.M. Grant, S. Krämer, G.G.E. Seward, and C.G. Levi, "Calcium–magnesium alumino-silicate interaction with yttrium monosilicate environmental barrier coatings," *J. Am. Ceram. Soc.,* **93[10]** 3504-3511. (2010).
16. A. Chesnaud, O. Joubert, M.T. Caldes, S. Ghosh, Y. Piffard, and L. Brohan, "Cuspidine-like compounds $Ln_4[Ga_{2(1-x)}Ge_{2x}O_{7+x}\square_{(1-x)}]O_2$ (Ln=La,Nd,Gd; x <= 0.4)," *Chem. Mater.,* **16[25]** 5372-5379. (2004).

17. S. Saburi, A. Kawahara, C. Henmi, I. Kusachi, and K. Kihara, "The refinement of the crystal structure of cuspidine," *Mineralogical Journal,* **8[5]** 286-298. (1977).
18. I. Warshaw and R. Roy, "New Family of Rare Earth Compounds," *Inorg. Chem.,* **1[3]** 719-&. (1962).
19. U. Kolitsch, H. Seifert, and F. Aldinger, "Phase relationships in the systems RE_2O_3-Al_2O_3-SiO_2 (RE = rare earth element, Y, and Sc)," *J. Phase Equilib.,* **19[5]** 426-433. (1998).
20. U. Kolitsch, H.J. Seifert, T. Ludwig, and F. Aldinger, "Phase equilibria and crystal chemistry in the Y_2O_3-Al_2O_3-SiO_2 system," *J. Mater. Res.,* **14[2]** 447-455. (1999).
21. S. Krämer and C.G. Levi, *Unpublished Data.* (2007).
22. H. Zhao, C.G. Levi, and H.N.G. Wadley, "Molten Silicate Interactions with Thermal Barrier Coatings," *Submitted for Review.* (2013).
23. N. Chellah, "Contribution à la compréhension de la dégradation chimique de barrières thermiques en zircone yttriée par les CMAS en vue de proposer une nouvelle composition céramique résistante dans le système ZrO_2-Nd_2O_3," *PhD Dissertation, Université de Lorraine.* (2013).
24. E. Zaleski, "Mechanisms and Mitigation of CMAS Attack on Thermal Barrier Coatings," *PhD Dissertation, University of California Santa Barbara.* (2013).
25. K. Kowalski, A. Bernasik, and A. Sadowski, "Diffusion of calcium in yttria stabilized zirconia ceramics," *J. Eur. Ceram. Soc.,* **20[12]** 2095-2100. (2000).

Contribution to Human resources

This program sponsored research performed by the following students:

- Kendra M. Grant, who received her Ph.D. in 2010 fully sponsored under this project. Her thesis did the pioneering work on the interaction of CMAS with BSAS and YMS, summarized in two publications. Upon graduation Dr. Grant worked for Apple in Cupertino, CA, as the principal materials engineer for displays. She is currently at Micron in Boise, ID, working as a materials engineer.
- David L. Poerschke, who received his Ph.D. in 2014 sponsored by an NDSEG fellowship for 3 years. His research expenditures were supported by this project with additional funding for part of the time from an AFOSR-STTR. After his NDSEG he was supported by this grant and then by ONR grant N00014-08-1-0522. His thesis covered a wide range of issues related to the architecture of advanced EBCs, including the development of robust SiC matrices and the interaction of CMAS with multilayer architectures. He has published 4 papers acknowledging this grant. Dr. Poerschke is current a post-doctoral associate at UCSB working primarily in an ONR STTR with QuesTek Innovations and also involved informally in ONR N000-14-14-1-0625. He intends to pursue an academic career and will start interviewing for faculty positions in Fall 2015.
- Dr. Steffen Burk, who was a visiting post-doctoral fellow with the PI, sponsored by the Humboldt Foundation. He worked on developing laboratory methods to synthesize multilayer architectures, characterize the thermal expansion of the constituents and a limited number of experiments on CMAS interactions. He is currently working at Isabellenhuette Heusler GmbH & Co, Dillenburg, Germany.
- Kimberly Wong, who received a B.Sc. in the College of Creative Studies at UCSB and worked as an undergraduate intern with D.L. Poerschke. She currently works for Agilent Technologies in Folsom, CA.
- Luke Merrill, who received a B.Sc. from UCSB and worked as an undergraduate intern while he was at Santa Barbara City College with D.L. Poerschke.
- Craig Patton was a high school student when he did an internship with D.L. Poerschke at UCSB. He then moved to get a degree at Cal State Fresno.

- Alex Pieman was also a high school student who did an internship with D.L. Poerschke at UCSB. He is now pursuing a degree at UC Davis.

Publications

This grant had two funding increments. The publications listed include both periods.

1. "CMAS Degradation of Environmental Barrier Coatings," K.M. Grant, S. Krämer, J.P.A. Löfvander, C.G. Levi, Surface and Coatings Technology 202 (4-7) 653-657 (2007).
2. "CMAS Interaction with Yttrium Monosilicate Environmental Barrier Coatings," K.M. Grant, S. Krämer, G.G.E. Seward and C.G. Levi, Journal of the American Ceramic Society 93 [10] 3504-3511 (2010).
3. "Yttrium bearing silicon carbide matrices for robust ceramic composites," David L. Poerschke and Carlos G. Levi, Journal of the American Ceramic Society, 96 [4] 1300-1308 (2013).
4. "Thermochemical Compatibility of Ytterbia-(Hafnia/Silica) Multilayers for Environmental Barrier Coatings," David L. Poerschke, Jason S. Van Sluytman, Kimberly Wong, Carlos G. Levi, Acta Materialia 61 (2013) 6743-6755.
5. "Stability and CMAS resistance of Ytterbium-silicate/hafnate TBC/EBCs for SiC composites," David L. Poerschke, Derek D. Hass, Susie Eustis, Gareth G.E. Seward, Jason Van Sluytman, Carlos G. Levi, Journal of the American Ceramic Society 98 [1] 278-286 (2015).
6. "Effect of cation substitution and temperature on the interaction between thermal barrier oxides and molten CMAS," David L. Poerschke and Carlos G. Levi, Journal of the European Ceramic Society 35 (2015) 681-691.

Numerous technical presentations including work performed under this grant have been given at national and international conferences by the PI and former students Poerschke and Grant, most recently a presentation on the work on robust matrices at the ECI conference on Ultra High Temperature Ceramics in Australia. In addition, the PI has given presentations at various academic institutions and industrial organizations, including GE Research, GE Aviation, Siemens Corporate Technology, and most recently at Aachen University, Forschungszentrum Jülich, TU Darmstadt and Karlsruhe Institute of Technology. A list can be provided if needed.